

Article

In-Situ Plasticized LLZTO-PVDF Composite Electrolytes for High-Performance Solid-State Lithium Metal Batteries

Xinjie Yu, Pengbo Zhai *, Ning Zhao  and Xiangxin Guo * 

College of Physics, Qingdao University, Qingdao 266071, China

* Correspondence: woshizpb@qdu.edu.cn (P.Z.); xxguo@qdu.edu.cn (X.G.)

Abstract: Solid polymer electrolytes (SPEs) are seen as the key component in the development of solid-state lithium batteries (SSLBs) by virtue of their good processability and flexibility. However, poor mechanical strength, low room-temperature lithium-ion (Li-ion) conductivity and unsatisfactory interfacial compatibility with electrodes limit their practical application. In this work, a composite electrolyte consisting of polyvinylidene fluoride and polyvinylidene carbonate with a $\text{Li}_{6.4}\text{La}_3\text{Zr}_{1.4}\text{Ta}_{0.6}\text{O}_{12}$ (LLZTO) active filler (PFPC: LLZTO-SPE) is reported to achieve excellent ionic conductivity ($4.25 \times 10^{-4} \text{ S cm}^{-1}$ at 30°C), a wide electrochemical window ($>4.6 \text{ V}$), a high Li-ion transference number ($t_{\text{Li}^+} = 0.49$) and good interfacial compatibility with the electrode. Incorporating LLZTO as an active filler not only increases the ionic conductivity of the electrolyte, but also homogenizes Li-ion flux and stabilizes the electrode/electrolyte interface, thereby preventing lithium dendrites from piercing the electrolyte. As a result, Li/Li symmetrical cells using PFPC: LLZTO-SPEs deliver more than 800 h of cyclability at 0.1 mA cm^{-2} and a high critical current density (CCD) of 2.6 mA cm^{-2} . The assembled Li/PFPC: LLZTO/LFP SSLBs achieve 87% capacity retention after 150 cycles at 0.2 C and 89% capacity retention for 100 cycles at 0.5 C. This work inspires new insights into designing high-performance SPEs.

Keywords: LLZTO; in-situ polymerization; solid polymer electrolytes; solid-state lithium batteries



Citation: Yu, X.; Zhai, P.; Zhao, N.; Guo, X. In-Situ Plasticized LLZTO-PVDF Composite Electrolytes for High-Performance Solid-State Lithium Metal Batteries. *Batteries* **2023**, *9*, 257. <https://doi.org/10.3390/batteries9050257>

Academic Editors: Atsushi Nagai and Johan E. ten Elshof

Received: 3 February 2023

Revised: 22 April 2023

Accepted: 26 April 2023

Published: 29 April 2023



Copyright: © 2023 by the authors. Licensee MDPI, Basel, Switzerland. This article is an open access article distributed under the terms and conditions of the Creative Commons Attribution (CC BY) license (<https://creativecommons.org/licenses/by/4.0/>).

1. Introduction

Lithium batteries show great application prospects in the field of energy storage due to their high energy density and low self-discharge rate [1,2]. At present, commercial Li-ion batteries based on volatile and flammable liquid electrolytes are gradually unable to fulfill the requirements of high energy density and high safety [3,4]. Solid-state lithium batteries (SSLBs) based on nonflammable solid-state electrolytes (SSEs), as the most promising choice of next-generation lithium batteries, have attracted extensive attention [5–7]. In addition, SSEs generally possess excellent electrochemical stability and can be used with high-voltage cathodes to produce high-energy-density batteries.

Common SSEs are mainly divided into inorganic solid electrolytes and organic solid polymer electrolytes. The inorganic SSEs possess the advantage of high room-temperature Li-ion conductivity and high mechanical strength, but significant hardness and brittleness induce large interfacial resistance with electrodes, which limits their practical applications [8–10]. Solid polymer electrolytes (SPEs) show high flexibility and good interfacial contact with electrodes, but relatively low room-temperature Li-ion conductivity makes them fail to meet the demand of high-energy-density lithium batteries [11–13]. Inorganic solid electrolyte powders such as $\text{Li}_7\text{La}_3\text{Zr}_2\text{O}_{12}$ (LLZO), $\text{Li}_{0.33}\text{La}_{0.56}\text{TiO}_{3-x}$ (LLTO) and $\text{Li}_{1.4}\text{Al}_{0.4}\text{Ti}_{1.6}(\text{PO}_4)_3$ (LATP) are introduced as active fillers, while the segmental motion of polymer chains is promoted by reducing the crystallinity of polymers through the interaction between the polymer and the inorganic material surface electrolyte. Thus, the resistance to Li dendrites is enhanced, and the conductivity of Li ions and the mechanical properties of the electrolyte are improved [14–17]. In addition, some functional groups

can help dissociate lithium salts based on Lewis acid-base interactions and increase Li-ion transfer. Up to now, significant efforts have been devoted to developing composite electrolytes composed of a polyethylene oxide (PEO) matrix and nano-sized inorganic solid electrolyte filler to achieve improved overall performance, and certain progress has been made [18]. However, the PEO matrix can be oxidized and decomposed at about 4 V (vs. Li/Li⁺), which restricts the application of PEO-based composite electrolytes in high-voltage scenarios [19]. Compared with PEO, poly(vinylidene fluoride) (PVDF) shows a wide electrochemical window to match high-voltage cathodes [20–22]. However, PVDF-based SPE film consists of a large number of micro-sized spherical particles due to solvent evaporation, thus creating voids inside the electrolyte film. These internal voids reduce the mechanical strength of the electrolyte and induce the uneven internal transport of Li ions, leading to lithium dendrite growth and puncturing of the electrolyte film [23]. Moreover, the presence of solvent molecules in the free state in the PVDF-based SPEs will result in interfacial deterioration due to side reactions with lithium metal [24]. Although high-temperature drying can remove the residual solvent and reduce the gap between PVDF polymer particles, it will also damage the structure of solvated Li ions, resulting in a sharp decrease in Li-ion conductivity [23,25]. In situ polymerization is an effective way to solve the existing problems of PVDF-based SPEs, such as low conductivity and interfacial instability [26–28]. First, the liquid polymerization precursor can penetrate between the electrode and the PVDF-based SPE, which effectively improves the solid-solid interfacial contact. In addition, an electrolyte constructed via in situ polymerization is relatively dense, which can produce uniform and dense ion transport paths [29–31]. In recent years, electrolytes based on in-situ solidification of vinylene carbonate (VC) monomers have been widely utilized [32]. For instance, Cui et al. designed a PVCA SPE supported by a cellulose matrix, which obtained an ionic conductivity of $9.82 \times 10^{-5} \text{ S cm}^{-1}$ at 50 °C [33]. Chen et al. reported a PVC-based SPE via in situ polymerization, achieving a superior ionic conductivity of $1.2 \times 10^{-4} \text{ S cm}^{-1}$ at 25 °C and good interfacial compatibility with electrodes [34]. However, the Li-ion transport in in-situ-polymerized pure PVC electrolytes relies on chain segments with a low degree of polymerization, which leads to unsatisfactory lithium dendrite resistance and a low Li-ion transference number. Moreover, inert supports such as glass fibers and polyolefins are unable to participate in Li-ion transport, resulting in a non-uniform distribution of Li-ion flux in the composite electrolytes [30,35,36]. Using a PVDF inorganic filler composite electrolyte as the substrate and incorporating an in-situ-polymerized PVC electrolyte is an effective but rarely reported method to solve the above problems and obtain a high-performance composite electrolyte [37–39].

Herein, we designed a composite solid polymer electrolyte with a PVDF/LLZTO composite electrolyte as the active substrate and PVC/LLZTO as the in-situ plasticizer to achieve superior comprehensive performance. In this design, the LLZTO particles as active fillers compounded with PVDF construct organic-inorganic interfaces to obtain rich ion transport paths, so that the PVDF polymer substrates effectively participate in Li-ion transport. Meanwhile, the LLZTO particle compounded with an in-situ-polymerized PVC electrolyte not only promotes the movement of polymer chains to improve Li-ion conductivity, but the electrochemical potential difference between the PVC and LLZTO also causes the migration of Li ions in the LLZTO lattice from the surface of LLZTO to the PVC, resulting in the formation of abundant lithium vacancies for rapid Li-ion transport. The LLZTO filler provides abundant Lewis's acid sites to adsorb anionic groups in the electrolyte, thereby increasing the Li-ion transference number. The resulting PVDF/PVC/LLZTO solid polymer electrolyte (PFPC: LLZTO-SPE) achieves a high Li-ion conductivity of $5.0 \times 10^{-4} \text{ S cm}^{-1}$ at room temperature, a broad electrochemical window of more than 4.6 V and a high Li-ion transference number of ~0.5. Moreover, the introduction of LLZTO ceramic additives effectively improves the comprehensive mechanical properties of the composite electrolyte, thereby inhibiting the penetration of lithium dendrites. As a result, the Li/Li symmetrical cells assembled with the PFPC: LLZTO-SPEs exhibit stable cycling for more than 800 h at 0.1 mA cm⁻² and a high critical current density (CCD) of 2.6 mA cm⁻². The

Li/LFP cells show stable cycling performance (capacity retention of more than 87% at 0.2 C for 150 cycles) and excellent rate capability (specific capacity of 103 mAh g⁻¹ at 2.0 C). This work explores the application of active fillers in composite electrolytes, which is an important guidance for large-scale synthesis of high-performance solid lithium batteries.

2. Materials and Methods

2.1. Materials for Experiment

Lithium difluoroxalate (LiDFOB, 99%, Aladdin, Shanghai, China), vinylene carbonate (VC, 98%, Aladdin), azodiisobutyronitrile (AIBN, 98%, Aladdin), LiOH·H₂O (99%, Aladdin), La(OH)₃ (99.99%, Aladdin), ZrO₂ (99.99%, Aladdin), Ta₂O₅ (99.99%, Aladdin), N-Methylpyrrolidone (NMP, 99.5%, Aladdin) and N,N-Dimethylformamide (DMF, 99.5%, Aladdin) were purchased and used without further purification. Polyvinylidene fluoride (PVDF, M_w = 500,000, Suweil 5130), lithium iron phosphate (LFP, Betri, Lyon, France), lithium metal foils and Super P carbon black were supplied by MTI Corporation.

2.2. Preparation of Electrolyte Support System

Based on previous work, the Li_{6.4}La₃Zr_{1.4}Ta_{0.6}O₁₂ (LLZTO) electrolyte powders were synthesized using the solid phase method. [27,40] The average particle size of the LLZTO obtained was about 500 nm. The preparation of electrolytes was carried out in an ultra-dry chamber with a dew point of -60 °C. Firstly, 0.12 g of LLZTO particles were dispersed in 8 mL DMF, which was evenly dispersed in DMF after ultrasonic and stirring. Then, 1 g of PVDF and 0.5 g of LiDFOB were dissolved in an LLZTO/DMF dispersion solution and stirred for 12 h to get a uniform slurry. Finally, the slurry was coated onto the glass plate using the solution pouring method, put in the vacuum oven and dried at 80 °C for 24 h to get a PVDF/LiDFOB/LLZTO SPE substrate. For comparison, the PVDF/LiDFOB SPE substrate without LLZTO was prepared using the same method.

2.3. Preparation of Polymerization Precursors

Firstly, different amounts (1, 3, or 5 wt%) of LLZTO were added to 1 mL VC solution, and the LLZTO powder was dispersed evenly under ultrasonic and stirring. Then, 0.144 g of LiDFOB and 0.005 g of AIBN were added and stirred for 1 h to obtain the polymeric precursor solution. In comparison, a VC polymeric precursor solution without LLZTO powder was also prepared. The precursor solution was added to the PVDF:LLZTO SPEs. These SPE membranes after polymerization were referred to as PFPC: 1 wt% LLZTO, PFPC: 3 wt% LLZTO and PFPC: 5 wt% LLZTO, respectively.

2.4. Preparation of Batteries

A lithium symmetrical CR 2032 battery was assembled through dropping 10 µL precursor solution on both sides of a 19 mm diameter SPE membrane support and a lithium foil. For a full battery, lithium iron phosphate was chosen as the positive terminal. The LFP positive electrode was prepared via solution casting. 80 wt% LFP, 10 wt% Super P and 10 wt% polyvinylidene fluoride (PVDF) were added to the NMP and stirred for 12 h to achieve a uniform slurry. The mass loading of the LFP was 5 ± 0.2 mg cm⁻². Further drying at 80 °C for 12 h was conducted. Lithium metal was used as the negative electrode. The prepared cell was heated in the oven at 60 °C for 24 h to complete the polymerization of the VC. All cells were assembled in a glove box filled with argon gas. Other electrochemical testing cells use the same method to replace the electrodes with stainless steel or lithium metal.

2.5. Electrochemical Test

SS/electrolyte/SS cells were assembled using stainless steel plates as blocking electrodes. Electrochemical impedance spectroscopy (EIS) was tested using an electrochemical

workstation (Princeton, NJ, USA). The test frequency was 1 MHz~0.1 Hz, and the temperature range was 30~60 °C. The calculation formula for ionic conductivity is:

$$\sigma = \frac{L}{R \cdot S} \quad (1)$$

where L is the thickness of electrolyte film, R is the EIS measurement result of the SS/electrolyte/SS cell, and S is the area of the SS electrode.

The transfer number of Li ions (t_{Li^+}) was measured using the DC polarization method of a Li/Li symmetrical cell with voltage polarization of 10 mV. t_{Li^+} is calculated according to the formula:

$$t_{Li^+} = \frac{I_s(\Delta V - I_i R_i)}{I_i(\Delta V - I_s R_s)} \quad (2)$$

where I_s and R_s represent the current and resistance of the Li/Li symmetric cell at the steady state, I_i and R_i represent the current and resistance of the Li/Li symmetric cell at the initial state and ΔV represents the voltage polarization applied. An SS/electrolyte/Li cell was assembled using a stainless steel sheet as the working electrode and lithium metal as the reference electrode. Electrochemical stability was tested via linear sweep voltammetry (LSV) using a Li/electrolyte/SS cell from 0 to 6 V.

2.6. Materials Characterization

The crystal structure of LLZTO was analyzed via X-ray diffraction (XRD) (Bruker D2 phaser, Cu K α radiates in the 2 θ range of 10~80° and a step size of 0.1°). The morphology of the electrolyte was measured using emission scanning electron microscopy (SEM) (FESU4800, Hitachi, Tokyo, Japan). Fourier transform infrared spectroscopy was performed using the Spectra Tech Collector II attachment in diffuse reflection mode with the Bruker Vertex V70 spectrometer. A gel permeation chromatography (GPC) investigation was performed using a Waters 1515 HPLC with three Styragel columns (HT3, HT4 and HT5) and 2414 differential refractive index detector. The eluant was Tetrahydrofuran (1 mL min⁻¹). Polystyrene standards were employed for the GPC calibration curve.

3. Results

3.1. Preparation and Physical Characterization of Electrolytes

Figure 1a shows the schematic preparation process of PFPC-based SPEs. Typically, a homogeneous precursor consisting of VC, LLZTO, lithium salt (LiDFOB) and azobisisobutyronitrile (AIBN) was dropped onto the PVDF-based polymer film, followed by heating at 60 °C to trigger the polymerization of the VC monomer and thus obtain the integrated composite solid polymer electrolyte (denoted as PFPC: LLZTO SPE). The PVDF/PVC solid polymer electrolyte (PFPC SPE) was synthesized for contrast using the same method, except that no LLZTO powder was added during the preparation process. As shown in Figure 1b, both VC and VC-LLZTO are in a liquid state in the initial stage, but are polymerized into a solid state after being heated at 60 °C. The results of the Fourier transform infrared (FTIR) spectroscopy (Figures 1c and S1) show that the intensity of the absorption peaks located at about 3160 and 1560 cm⁻¹, corresponding to the C=C-H and C=C bonds, in the PVC and PVC: 3 wt% LLZTO is significantly weaker than that of the VC and VC: 3 wt% LLZTO, which indicates the successful polymerization of the VC monomers. The results of the gel permeation chromatography (GPC) test show the average molecular weight ($M_n = 178,949$) and the average molar mass ($M_w = 405,818$) of the PVC after polymerization, which further indicate that the PVC had a high degree of polymerization (Figure S2).

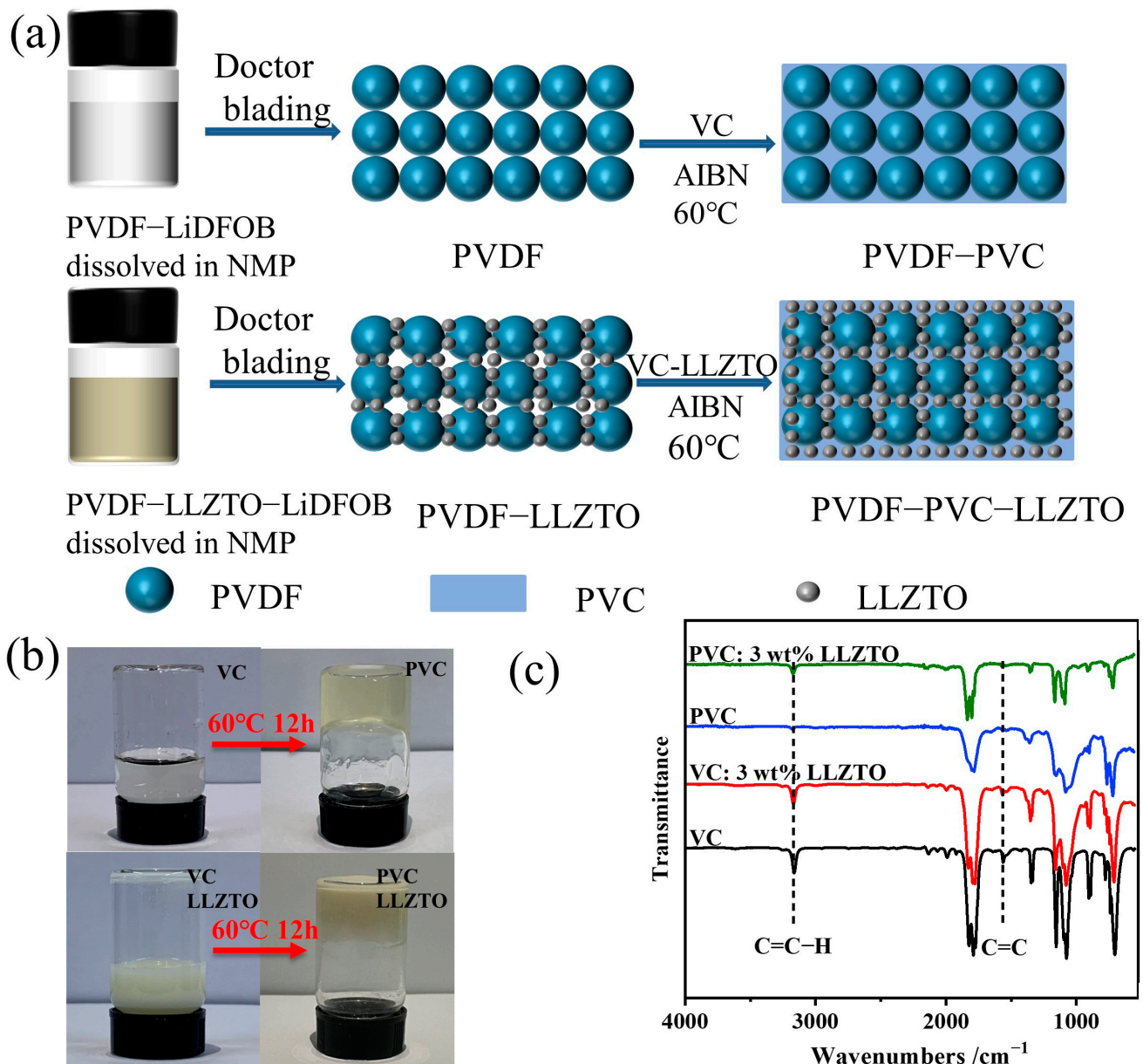


Figure 1. (a) Schematic illustration of the preparation process of PFPC SPEs and PFPC: 3 wt% LLZTO SEPs via in situ polymerization. (b) Photographs of VC, PVC, VC: LLZTO and PVC: LLZTO. (c) FTIR spectra of VC, PVC, VC: 3 wt% LLZTO and PVC: 3 wt% LLZTO SPEs.

The particle size of fillers has a great influence on the performance of composite electrolytes [18,40]. The nanoscale inorganic fillers in the composite electrolyte build fast ion transport paths, and the larger the specific surface area of the particles, the stronger the interaction between the polymer-free matrix or lithium salt and the more interfaces for ion migration, thus improving the Li-ion conductivity of the electrolyte. Nanoscale inorganic fillers in composite electrolytes build increased interfaces with fast ion transport paths, which improve the Li-ion conductivity of electrolytes [41,42]. The size distribution test (Figure 2a) shows that the D_{10} , D_{50} and D_{90} sizes of LLZTO fillers are 0.166 μm , 0.518 μm and 1.106 μm , respectively. The scanning electron microscope (SEM) measurements presented in Figures 2b and S3 further demonstrate that the LLZTO particles are evenly dispersed, with the diameter concentrating at approximately 500 nm. The X-ray diffraction (XRD) pattern indicates that the LLZTO fillers present a cubic-phase structure with high ionic conductivity. The XRD pattern of the PFPC SPE obtained via in situ polymerization

is similar to that of the pure PVDF (PF) film, and no characteristic peaks corresponding to lithium salts can be observed, indicating that the lithium salts are fully dissociated in the SPEs. Moreover, the characteristic peaks of LLZTO appear in the XRD pattern of the PFPC: 3 wt% LLZTO, indicating the successful introduction of the LLZTO fillers into the SPEs (Figure 2c). As shown in Figure S4, the PVDF SPEs without LLZTO have more voids than PVDF: LLZTO SPEs. It can be observed in Figure 2d,e that compared to the loose structure of PVDF: LLZTO SPEs, the pores of PFPC: LLZTO SPEs are filled by the in-situ-polymerized PVC: LLZTO to form a continuous texture. The loose structure limits the improvement of ionic conductivity and interface compatibility, and the compact structure is expected to solve these problems. Figure S5 shows that the PVDF: LLZTO SPE film exhibits excellent flexibility, which enables it to be folded at any angle. This property remains unchanged after in situ polymerization to form the PFPC: 3 wt% LLZTO SPE (as shown in Figure 2f). Figures 2g and S6 show that the thickness of the PFPC: 3 wt% LLZTO SPE is $\sim 50 \mu\text{m}$ and the EDS mapping shows the uniform distribution of C, F, O and Zr elements, indicating the LLZTO and LiDFOB are uniformly distributed in the PFPC: 3 wt% LLZTO SPE. These excellent structural properties of the composite electrolyte lay the foundation for the improvement of electrochemical performance.

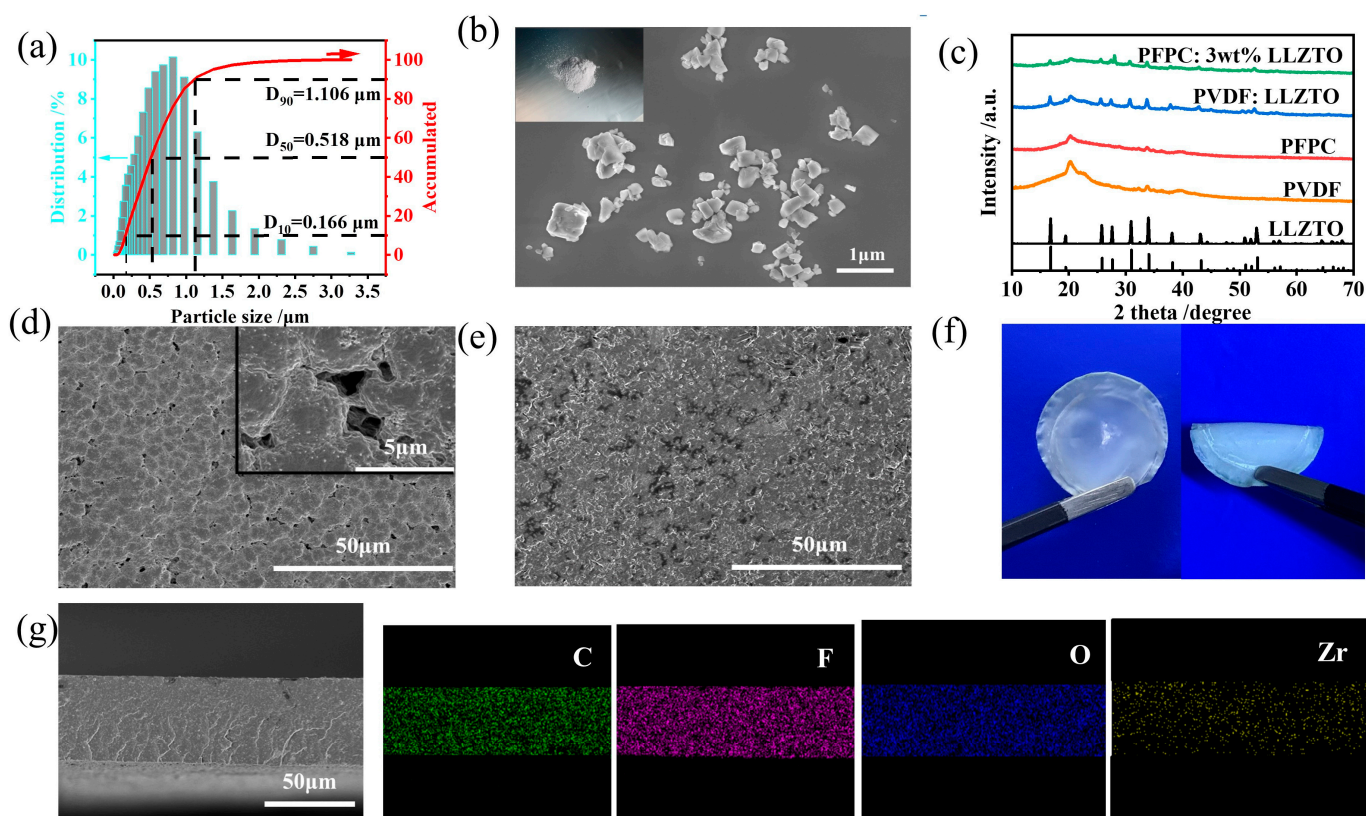


Figure 2. (a) Size distribution of the LLZTO determined using a laser particle size analyzer. (b) SEM photo of LLZTO nanoparticles and LLZTO powder. (c) XRD patterns of LLZTO, PVDF, PFPC, PVDF: LLZTO and PFPC: 3 wt% LLZTO. (d) SEM image of PVDF: LLZTO. The inset is the high-resolution SEM image of PVDF: LLZTO. (e) SEM image of PFPC: 3 wt% LLZTO. (f) PVDF: LLZTO SPEs after polymerization. (g) Cross-sectional SEM image and the corresponding elemental analysis of PFPC: 3 wt% LLZTO SPEs.

3.2. Electrochemical Performance of Electrolytes

Using stainless steel sheets as blocking electrodes to assemble symmetrical cells, an electrochemical impedance spectroscopy (EIS) test was carried out through the electrochemical workstation. Based on the EIS spectra in Figure 3a, the resistance value of PFPC: 3 wt% LLZTO SPE is 6.16Ω at $30 \text{ }^\circ\text{C}$ and the unit area resistance is $3.22 \Omega \text{ cm}^{-2}$. The

Li-ion conductivity can be calculated to be $4.25 \times 10^{-4} \text{ S cm}^{-1}$ via referring to Formula 1. As shown in Figure 3b, the Li-ion conductivity of the PFPC SPE without LLZTO is $1.82 \times 10^{-4} \text{ S cm}^{-1}$ at 30°C and can be significantly improved via adding an LLZTO active filler, among which the PFPC: 3 wt% LLZTO SPE shows the highest Li-ion conductivity of $4.25 \times 10^{-4} \text{ S cm}^{-1}$. This is attributed to the fact that PVC with LLZTO fills the internal pores of PVDF and forms a new fast ion transport channel at the interface between PVC and LLZTO after the addition of LLZTO fillers. The inherent polarity of PVDF is weak, which results in its poor ability to dissociate lithium salts. As a result, a pure PVDF-lithium salt system is unable to conduct Li ions. In PVDF-based SPEs, lithium ions are transported through the interactions between the [solvent-Li⁺] complex (solvated Li ion) and the polymer [22,43]. When LLZTO is introduced into the PVDF-based SPE, a new interface is formed between PVDF and LLZTO, which enables fast transport of solvated Li ions. For the PVC: LLZTO SPEs, the electrochemical potential difference between the PVC and LLZTO causes the migration of Li ions in the LLZTO lattice from the surface of the LLZTO to the PVC, resulting in the formation of a large number of lithium vacancies for rapid lithium-ion transport [18,44]. However, high LLZTO content may lead to particle agglomeration and hinder ion transport, resulting in reduced ionic conductivity. PFPC: 3 wt% LLZTO SPE was used in the subsequent tests. The ionic transference in the electrolyte was divided into cation (Li⁺ in this case) and anion (DFOB⁻ in this case) transference, where the effective ionic transference is the transference of Li ions. A high Li-ion transference number is beneficial for improving the effective Li-ion conductivity of the electrolyte. The Li-ion transference number (t_{Li^+}) of the PFPC: 3 wt% LLZTO calculated from the Bruce-Vincent-Evans equation is 0.49 (Figure 3d), higher than that of the PFPC ($t_{\text{Li}^+} = 0.16$, Figure 3c), which is due to the introduction of LLZTO [16]. The LLZTO filler dissociates lithium salts through using Lewis acid-base interaction on the surface, adsorbs the anion group and improves the efficiency of Li-ion transport at the same time. Linear scanning voltammetry (LSV) was used to test the electrochemical stability of the electrolyte. As shown in Figure S7, the PFPC SPE starts oxidative decomposition at 3.0 V, which can be attributed to the oxidation of the unpolymerized VC [45]. The electrochemical window was raised to 4.6 V after the introduction of LLZTO particles in PVDF and PVC. After adding LLZTO nanoparticles, the internal specific surface area of the electrolyte increased, leading to a uniform electric field [21]. A uniform electric field can increase the stability of the composite electrolyte under high voltage. This result indicates that the PFPC: 3 wt% LLZTO SPE possesses the capability to match the high-voltage cathode.

3.3. Stability against Electrolytes for Lithium Metal

The stability of the Li/electrolyte interface is the key to an SSLB's cycle performance. The Li/electrolyte interface was evaluated through assembling Li/Li symmetrical cells. As shown in Figure 4a, the polarization voltage of the PFPC: 3 wt% LLZTO SPE is significantly lower than that of the PFPC SPE at the same current density. The Li/PFPC: 3 wt% LLZTO/Li symmetrical cell cycles stably for 800 h at 30°C under 0.1 mA cm^{-2} , while the Li/PFPC/Li symmetrical cell short-circuits after only 100 h. The interface resistance can directly reflect the interface stability. The EIS of the Li/Li symmetric cells before and after cycling is shown in Figure 4b,c. The semicircle can be simulated via the inset model circuit in Figure 4b,c. Both spectra consist of a tiny semicircle which can be ascribed to the overall resistance of the electrolyte (bulk resistance) at high frequencies (R1), and a large semicircle which can be resolved to the interface resistance between lithium metal and the electrolyte film (R2) as well as the interface resistance between the internal components (PVDF substrate and the PVC: LLZTO) of the electrolyte (R3) [46,47]. After 100 cycles, the initial interface resistance of the Li/PFPC/Li cell is 263Ω ($337 \Omega \text{ cm}^{-2}$), which is impossible to measure using a reasonable EIS, indicating that a short circuit occurs in the Li/PFPC/Li cell. By contrast, the interface resistance of the Li/PFPC: 3 wt% LLZTO/Li cell only increases from 127Ω ($163 \Omega \text{ cm}^{-2}$) to 194Ω ($248 \Omega \text{ cm}^{-2}$) after 100 cycles. During the initial stages of cycling, the increase in impedance can be attributed to the formation

of an SEI at the interface between the lithium metal and the electrolyte. After long-term cycling, the increase in impedance is caused by the interfacial side reaction between the polymer components in the electrolyte and the lithium metal electrodes. This indicates that the introduction of LLZTO improves the stability of the electrolyte against lithium metal. The Li/PFPC: 3 wt% LLZTO/Li cell cycles stably for more than 600 h when the current density is increased to 0.2 mA cm^{-2} (Figure 4d). Figure 4e shows the rate performance of symmetric cells at various current densities. The Li/PFPC/Li cell suffers a short circuit at 1.6 mA cm^{-2} . This is due to the rapid growth of lithium dendrites under high current density, which results in the short circuit of the cell and a sharp voltage drop [27]. In comparison, Li/PFPC: 3 wt% LLZTO/Li delivers a much smaller voltage hysteresis at various current densities, and the cell maintains stable cycling under 2.3 mA cm^{-2} .

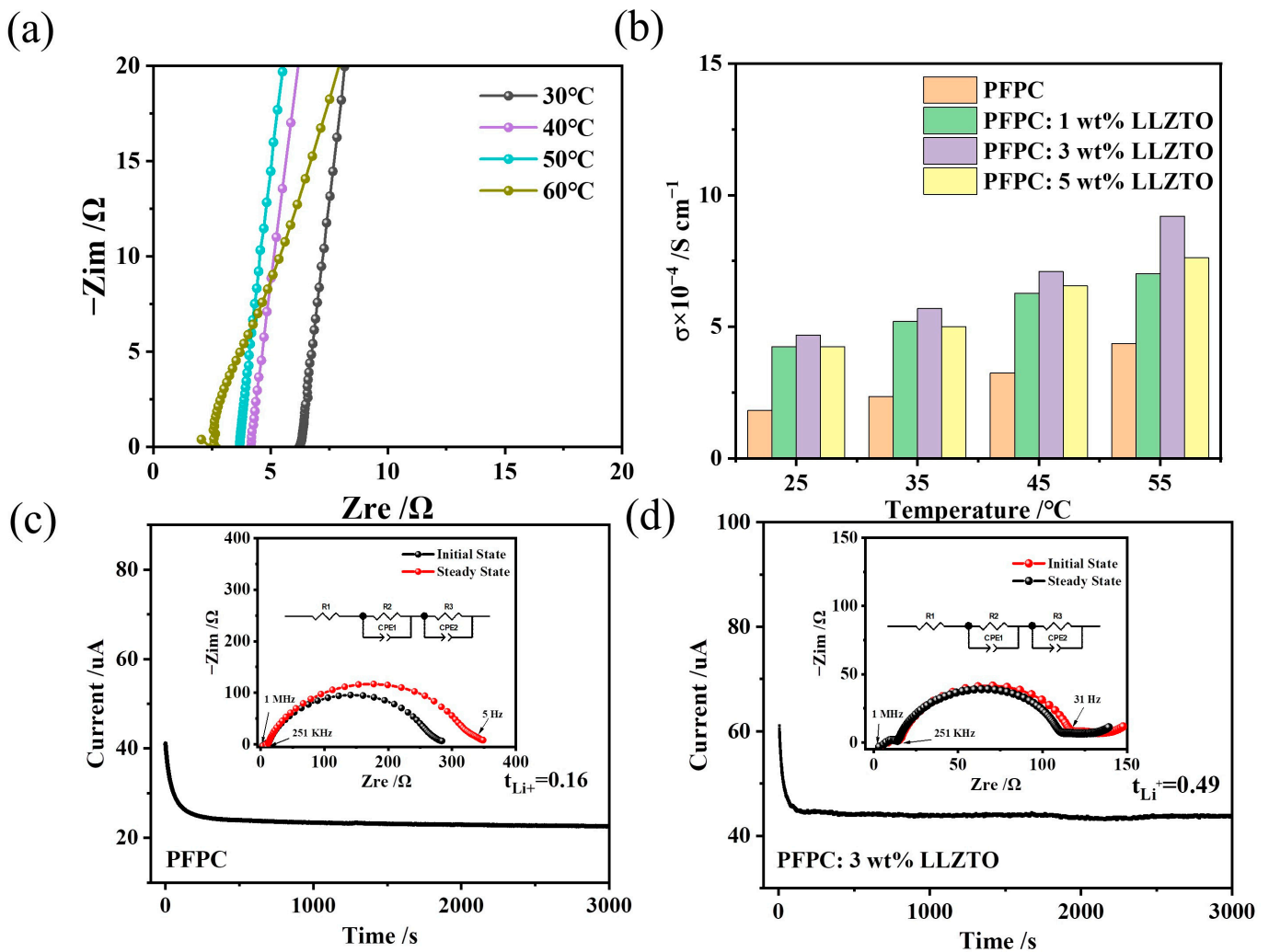


Figure 3. (a) EIS of PFPC: 3 wt% LLZTO SPEs at various temperatures. (b) Ionic conductivities of 1%, 3% and 5 wt % LLZTO/PVC composite electrolytes at 30 °C, 40 °C, 50 °C and 60 °C. (c) Current variation with time during polarization of a Li/PFPC/Li cell and (d) Li/PFPC: 3 wt% LLZTO/Li cell under 10 mV.

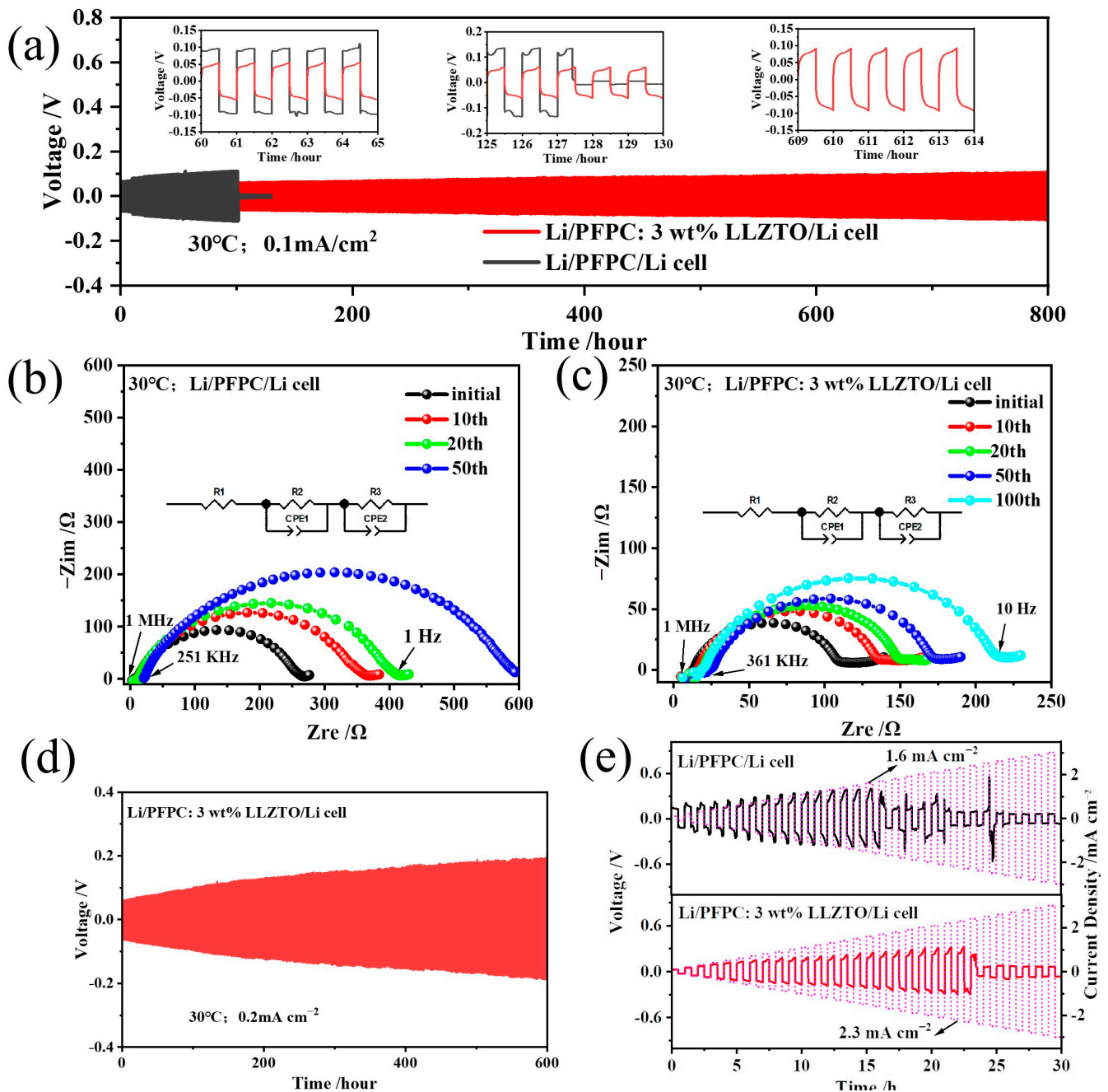


Figure 4. (a) Galvanostatic cycling curves of Li/PFPC: 3 wt% LLZTO/Li and Li/PFPC/Li cells under 0.1 mA cm^{-2} for 800 h. (b) EIS of Li/PFPC/Li measured at 30°C . (c) EIS of Li/PFPC: 3 wt% LLZTO/Li measured at 30°C . (d) Galvanostatic cycling curves of Li/PFPC: 3 wt% LLZTO/Li cells at the current density of 0.2 mA cm^{-2} for 600 h. (e) Galvanostatic charge/discharge curves of Li/PFPC/Li and Li/PFPC: 3 wt% LLZTO/Li cells at different current densities.

Excellent stability against lithium depends on the uniform deposition of lithium. Lithium deposition behavior is closely related to the transport process of Li ions. The main Li-ion transport path in the PFPC SPE is the PVC gel electrolyte in the PVDF pores, so the lithium dendrites grow in the PVDF pores (Figure 5a). When LLZTO nanoparticles are introduced into the polymer matrix, the electrochemical potential difference between the PVC and the LLZTO causes the migration of Li ions in the LLZTO lattice from the surface of the LLZTO to the PVC, resulting in the formation of a large number of lithium vacancies for rapid lithium-ion transport. During this process, a space charge layer is formed at

the interface between the polymer substrate and the LLZTO. The space charge layer at the interface of LLZTO and PVC can be used as a three-dimensional ion migration path to redistribute Li ions at the interface of the PFPC: 3 wt% LLZTO SPE and lithium metal anode, so as to achieve uniform lithium deposition on the surface of the lithium metal (Figure 5c) [48–51]. As shown in Figure 5b,d, after cycling for 100 h, the surface of the electrode in the Li/PFPC/Li cell becomes rough. In contrast, the surface of the electrode in the Li/PFPC: 3 wt% LLZTO/Li cell is still smooth and flat after 100 h of cycling. The excellent interfacial contact and stability between the Li metal and the PFPC: 3 wt% LLZTO SPE facilitates long-term cycling in cells.

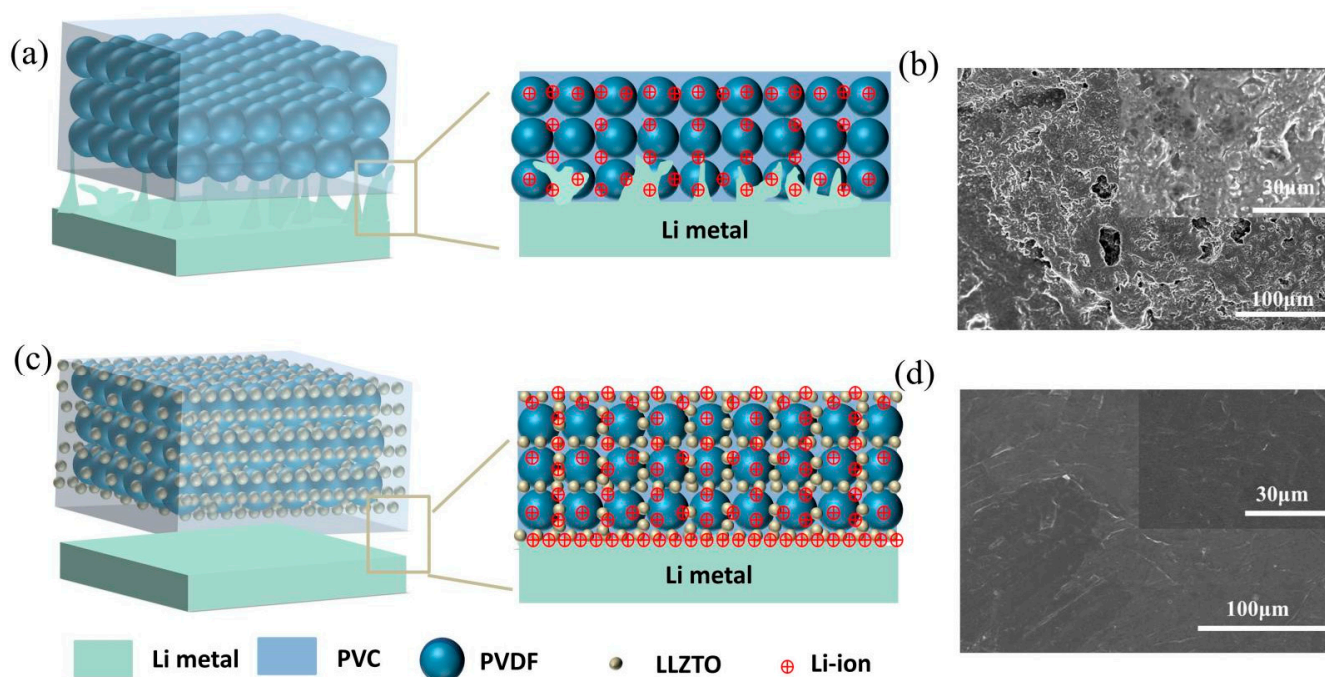


Figure 5. (a,c) Schematic illustration of the electrochemical deposition behaviors. The influence of PFPC and PFPC: 3 wt% LLZTO SPEs on Lithium metal deposition. (b,d) SEM image of electrode in Li/PFPC/Li and Li/PFPC: 3 wt% LLZTO/Li cell after 100th Li stripping.

3.4. Solid-State Battery Performance

In order to verify the application of electrolytes in practice, Li/LFP cells were assembled. The cells were subjected to cyclic voltammetry (CV) testing. Figure 6a shows the initial CV curves of the Li/PFPC: 3 wt% LLZTO/LFP cell; these five curves basically coincide. The peaks of the curve correspond to the Li-ion insertion and extraction behavior of LFP material, indicating good cycling performance of Li ions during the cycle and almost no loss during the cycle. Further, the cells were subjected to charge and discharge cycles between 2.5 and 3.8 V at room temperature to verify the application of the electrolyte. The rate performance of the Li/LFP cells is shown in Figure 6b,c. It can be seen that the capacity of the Li/PFPC: 3 wt% LLZTO/LFP cell is 156, 151, 140, 127 and 103 mAh g⁻¹ at 0.1, 0.2, 0.5, 1.0 and 2.0 C, respectively. When the current returns to 0.1 C, the capacity is restored to 154 mAh g⁻¹. The excellent rate capability benefits from the fast Li-ion transfer kinetics of PFPC: 3 wt% LLZTO SPEs. The smooth charge/discharge curves of the Li/PFPC: 3 wt% LLZTO/LFP cell at cycles of various rates indicate that no side reactions occur during the cell cycle. However, the polarization voltage of the cell increases slightly as the cycle rate increases, while the specific capacity decreases slightly. In contrast, the specific capacity of the Li/PFPC/LFP cell is 140 mAh g⁻¹ at 0.1 C. As the current density increases, the specific capacity decreases significantly to 23 mAh g⁻¹ at 2.0 C, and the charge/discharge curve shows that polarization of the cell increases significantly as the cycle rate increases (Figure S8). As shown in Figure 6d,e, the Li/PFPC: 3 wt% LLZTO/LFP cell cycles stably

for more than 150 cycles at 0.2 C (0.13 mA cm^{-2}) with a capacity retention rate of about 87% and an average coulomb efficiency of 99.5%. In contrast, the specific capacity of the LFP/PFPC/Li cell is only 27 mAh g^{-1} after 150 cycles at 0.2 C (0.15 mA cm^{-2}), and the charge/discharge curve of the cell shows that the polarization voltage of the cell increases significantly after cycling, which is caused by the side reactions between the Li metal and PVC at the interface (Figure S9). Further verifying the cycling performance of the Li/PFPC: 3 wt% LLZTO/LFP cell at a high rate, the stable cycling at 0.5 C (0.61 mA cm^{-2}) for more than 100 cycles results in a capacity retention rate of about 89% and a coulomb efficiency of 99.5% (Figure 6f,g). The much-improved electrochemical performance of the Li/PFPC: 3 wt% LLZTO/LFP cell benefits from the fast Li-ion transport of the electrolyte and the good interface contact between the electrolyte and the electrode, demonstrating the prospect of practical applications of the PFPC: 3 wt% LLZTO SPE.

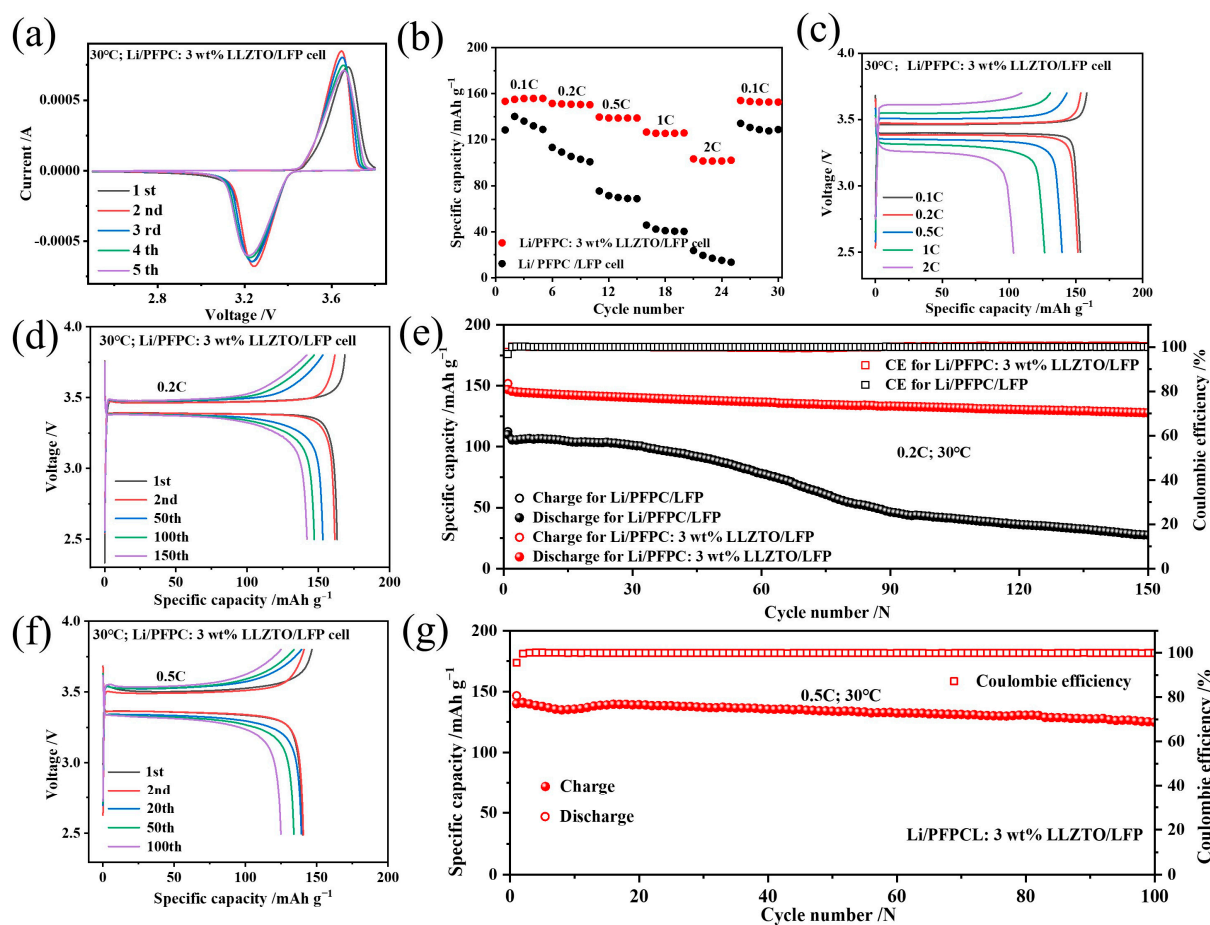


Figure 6. (a) Cyclic voltammetry of the Li/PFPC: 3 wt% LLZTO/LFP cell at 1 mV S^{-1} . (b) Rate capability of Li/PFPC: 3 wt% LLZTO/LFP and Li/PFPC/LFP cells. (c) Li/PFPC: 3 wt% LLZTO/LFP cells under different rates. (d) Charge/discharge curves of Li/PFPC: 3 wt% LLZTO/LFP at 0.2 C. (e) Cycling performance of Li/PFPC: 3 wt% LLZTO/LFP and Li/PFPC/LFP cells at 0.2 C. (f) Charge/discharge curves of Li/PFPC: 3 wt% LLZTO/LFP at 0.5 C. (g) Cycling performance of Li/PFPC: 3 wt% LLZTO/LFP cells at 0.5 C.

4. Conclusions

In this work, a novel PFPC: 3 wt% LLZTO SPE was fabricated via in situ polymerization. The introduction of VC and LLZTO not only filled the holes in the PVDF SPE, but also homogenized Li-ion flux and stabilized the electrode/electrolyte interface, thereby preventing lithium dendrites from piercing the electrolyte. This hybrid PFPC: 3 wt% LLZTO SPE exhibits improved ionic conductivity ($4.25 \times 10^{-4} \text{ S cm}^{-1}$ at 30°C), a broad electrochemical window ($>4.6 \text{ V}$) and a high Li-ion transference number ($t_{\text{Li}^+} = 0.49$). The

integrated Li/PFPC: LLZTO-SPE/LFP cells exhibit much-improved capacity retention and long cycling life. This work provides a promising strategy for composite electrolytes and offers prospects and directions for solid lithium metal batteries.

Supplementary Materials: The following supporting information can be downloaded at: <https://www.mdpi.com/article/10.3390/batteries9050257/s1>, Figure S1: FTIR spectra of VC, LLZTO and PVDF: LLZTO, Figure S2: The GPC curves of the PVC after polymerization, Figure S3: SEM images of as-synthesized LLZTO powder, Figure S4: SEM images of PVDF SPEs, Figure S5: PVDF: LLZTO SPEs before polymerization, Figure S6: EDX of PFPC: 3 wt% LLZTO SPE, Figure S7: Electrochemical stability of different SPEs. Linear sweep voltammetry (LSV) curves of Li/PFPC: 3 wt% LLZTO/SS (red line) and Li/PFPC/SS (black line) cells, Figure S8: Li/PFPC/LFP cells under different rates, Figure S9: Charge/discharge curves of Li/PFPC/LFP cell at 0.2 C.

Author Contributions: Conceptualization, X.Y., P.Z. and X.G.; methodology, X.Y.; validation, X.Y., P.Z. and N.Z.; formal analysis, X.Y.; investigation, X.Y., P.Z. and X.G.; resources, N.Z. and X.G.; data curation, X.Y. and P.Z.; writing—original draft preparation, X.Y.; writing—review and editing, X.G. and P.Z.; visualization, X.Y. and P.Z.; supervision, X.G.; project administration, N.Z.; funding acquisition, P.Z. and X.G. All authors have read and agreed to the published version of the manuscript.

Funding: This work was supported by the Key R&D Program of Shandong Province, China (Grant No. 2021CXGC010401), the National Natural Science Foundation of China (Grant No. U1932205, 52202259).

Institutional Review Board Statement: Not applicable.

Informed Consent Statement: Not applicable.

Data Availability Statement: The data presented in this study are available on request from the corresponding author.

Conflicts of Interest: The authors declare no conflict of interest.

References

1. Goodenough, J.B.; Kim, Y. Challenges for Rechargeable Li Batteries. *Chem. Mater.* **2009**, *22*, 587–603. [[CrossRef](#)]
2. Goodenough, J.B.; Park, K.S. The Li-ion rechargeable battery: A perspective. *J. Am. Chem. Soc.* **2013**, *135*, 1167–1176. [[CrossRef](#)]
3. Liu, B.; Jia, Y.; Li, J.; Yin, S.; Yuan, C.; Hu, Z.; Wang, L.; Li, Y.; Xu, J. Safety issues caused by internal short circuits in lithium-ion batteries. *J. Mat. Chem. A* **2018**, *6*, 21475–21484. [[CrossRef](#)]
4. Tarascon, J.M.; Armand, M. Issues and challenges facing rechargeable lithium batteries. *Nature* **2001**, *414*, 359–367. [[CrossRef](#)]
5. Chen, S.; Wen, K.; Fan, J.; Bando, Y.; Golberg, D. Progress and future prospects of high-voltage and high-safety electrolytes in advanced lithium batteries: From liquid to solid electrolytes. *J. Mat. Chem. A* **2018**, *6*, 11631–11663. [[CrossRef](#)]
6. Manthiram, A.; Yu, X.; Wang, S. Lithium battery chemistries enabled by solid-state electrolytes. *Nat. Rev. Mater.* **2017**, *2*, 16103. [[CrossRef](#)]
7. Jia, M.; Zhao, N.; Huo, H.; Guo, X. Comprehensive Investigation into Garnet Electrolytes Toward Application-Oriented Solid Lithium Batteries. *Electrochem. Electrochem. Energy Rev.* **2020**, *3*, 656–689. [[CrossRef](#)]
8. Zhao, N.; Khokhar, W.; Bi, Z.; Shi, C.; Guo, X.; Fan, L.-Z.; Nan, C.-W. Solid Garnet Batteries. *Joule* **2019**, *3*, 1190–1199. [[CrossRef](#)]
9. Huang, L.; Gao, J.; Bi, Z.; Zhao, N.; Wu, J.; Fang, Q.; Wang, X.; Wan, Y.; Guo, X. Comparative Study of Stability against Moisture for Solid Garnet Electrolytes with Different Dopants. *Energies* **2022**, *15*, 3206. [[CrossRef](#)]
10. Miao, X.; Guan, S.; Ma, C.; Li, L.; Nan, C.W. Role of Interfaces in Solid-State Batteries. *Adv. Mater.* **2022**, e2206402. [[CrossRef](#)]
11. Li, J.; Cai, Y.; Wu, H.; Yu, Z.; Yan, X.; Zhang, Q.; Gao, T.Z.; Liu, K.; Jia, X.; Bao, Z. Polymers in Lithium-Ion and Lithium Metal Batteries. *Adv. Energy Mater.* **2021**, *11*, 2003239. [[CrossRef](#)]
12. Zhou, D.; Shanmukaraj, D.; Tkacheva, A.; Armand, M.; Wang, G. Polymer Electrolytes for Lithium-Based Batteries: Advances and Prospects. *Chem* **2019**, *5*, 2326–2352. [[CrossRef](#)]
13. Choo, Y.; Halat, D.M.; Villaluenga, I.; Timachova, K.; Balsara, N.P. Diffusion and migration in polymer electrolytes. *Prog. Polym. Sci.* **2020**, *103*, 101220. [[CrossRef](#)]
14. Liu, S.; Liu, W.; Ba, D.; Zhao, Y.; Ye, Y.; Li, Y.; Liu, J. Filler-Integrated Composite Polymer Electrolyte for Solid-State Lithium Batteries. *Adv. Mater.* **2022**, *35*, e2110423. [[CrossRef](#)]
15. Fan, P.; Liu, H.; Marosz, V.; Samuels, N.T.; Suib, S.L.; Sun, L.; Liao, L. High Performance Composite Polymer Electrolytes for Lithium-Ion Batteries. *Adv. Funct. Mater.* **2021**, *31*, 2101380. [[CrossRef](#)]
16. Jia, M.; Muhammad, K.T.; Guo, X. Insight into the key factors in high Li⁺ transference number composite electrolytes for solid lithium batteries. *ChemSusChem* **2022**, *16*, e202201801. [[CrossRef](#)] [[PubMed](#)]

17. Lu, W.; Xue, M.; Zhang, C. Modified Li₇La₃Zr₂O₁₂ (LLZO) and LLZO-polymer composites for solid-state lithium batteries. *Energy Storage Mater.* **2021**, *39*, 108–129. [[CrossRef](#)]
18. Zhang, J.; Zhao, N.; Zhang, M.; Li, Y.; Chu, P.K.; Guo, X.; Di, Z.; Wang, X.; Li, H. Flexible and ion-conducting membrane electrolytes for solid-state lithium batteries: Dispersion of garnet nanoparticles in insulating polyethylene oxide. *Nano Energy* **2016**, *28*, 447–454. [[CrossRef](#)]
19. Mu, S.; Huang, W.; Sun, W.; Zhao, N.; Jia, M.; Bi, Z.; Guo, X. Heterogeneous electrolyte membranes enabling double-side stable interfaces for solid lithium batteries. *J. Energy Chem.* **2021**, *60*, 162–168. [[CrossRef](#)]
20. Zhang, X.; Wang, S.; Xue, C.; Xin, C.; Lin, Y.; Shen, Y.; Li, L.; Nan, C.W. Self-Suppression of Lithium Dendrite in All-Solid-State Lithium Metal Batteries with Poly(vinylidene difluoride)-Based Solid Electrolytes. *Adv. Mater.* **2019**, *31*, e1806082. [[CrossRef](#)]
21. Zhou, Z.; Sun, T.; Cui, J.; Shen, X.; Shi, C.; Cao, S.; Zhao, J. A homogenous solid polymer electrolyte prepared by facile spray drying method is used for room-temperature solid lithium metal batteries. *Nano Res.* **2021**, *16*, 5080–5086. [[CrossRef](#)]
22. Wu, Y.; Li, Y.; Wang, Y.; Liu, Q.; Chen, Q.; Chen, M. Advances and prospects of PVDF based polymer electrolytes. *J. Energy Chem.* **2022**, *64*, 62–84. [[CrossRef](#)]
23. Zhai, P.; Yang, Z.; Wei, Y.; Guo, X.; Gong, Y. Two-Dimensional Fluorinated Graphene Reinforced Solid Polymer Electrolytes for High-Performance Solid-State Lithium Batteries. *Adv. Energy Mater.* **2022**, *12*, 2200967. [[CrossRef](#)]
24. Zhang, X.; Han, J.; Niu, X.; Xin, C.; Xue, C.; Wang, S.; Shen, Y.; Zhang, L.; Li, L.; Nan, C.W. High Cycling Stability for Solid-State Li Metal Batteries via Regulating Solvation Effect in Poly(Vinylidene Fluoride)-Based Electrolytes. *Batter. Supercaps* **2020**, *3*, 876–883. [[CrossRef](#)]
25. Jie, J.; Liu, Y.; Cong, L.; Zhang, B.; Lu, W.; Zhang, X.; Liu, J.; Xie, H.; Sun, L. High-performance PVDF-HFP based gel polymer electrolyte with a safe solvent in Li metal polymer battery. *J. Energy Chem.* **2020**, *49*, 80–88. [[CrossRef](#)]
26. Ding, P.; Lin, Z.; Guo, X.; Wu, L.; Wang, Y.; Guo, H.; Li, L.; Yu, H. Polymer electrolytes and interfaces in solid-state lithium metal batteries. *Mater. Today* **2021**, *51*, 449–474. [[CrossRef](#)]
27. Bi, Z.; Huang, W.; Mu, S.; Sun, W.; Zhao, N.; Guo, X. Dual-interface reinforced flexible solid garnet batteries enabled by in-situ solidified gel polymer electrolytes. *Nano Energy* **2021**, *90*, 106498. [[CrossRef](#)]
28. Zhang, X.; Liu, T.; Zhang, S.; Huang, X.; Xu, B.; Lin, Y.; Xu, B.; Li, L.; Nan, C.W.; Shen, Y. Synergistic Coupling between Li_{6.75}La₃Zr_{1.75}Ta_{0.25}O₁₂ and Poly(vinylidene fluoride) Induces High Ionic Conductivity, Mechanical Strength, and Thermal Stability of Solid Composite Electrolytes. *J. Am. Chem. Soc.* **2017**, *139*, 13779–13785. [[CrossRef](#)] [[PubMed](#)]
29. Pan, J.; Zhang, Y.; Wang, J.; Bai, Z.; Cao, R.; Wang, N.; Dou, S.; Huang, F. A Quasi-Double-Layer Solid Electrolyte with Adjustable Interphases Enabling High-Voltage Solid-State Batteries. *Adv. Mater.* **2022**, *34*, e2107183. [[CrossRef](#)]
30. Wang, Z.; Shen, L.; Deng, S.; Cui, P.; Yao, X. 10 μm-Thick High-Strength Solid Polymer Electrolytes with Excellent Interface Compatibility for Flexible All-Solid-State Lithium-Metal Batteries. *Adv. Mater.* **2021**, *33*, e2100353. [[CrossRef](#)]
31. Li, Z.; Zhou, X.-Y.; Guo, X. High-performance lithium metal batteries with ultraconformal interfacial contacts of quasi-solid electrolyte to electrodes. *Energy Storage Mater.* **2020**, *29*, 149–155. [[CrossRef](#)]
32. Zhang, Q.; Liu, S.; Lin, Z.; Wang, K.; Chen, M.; Xu, K.; Li, W. Highly safe and cyclable Li-metal batteries with vinylene carbonate electrolyte. *Nano Energy* **2020**, *74*, 104860. [[CrossRef](#)]
33. Chai, J.; Liu, Z.; Ma, J.; Wang, J.; Liu, X.; Liu, H.; Zhang, J.; Cui, G.; Chen, L. In Situ Generation of Poly (Vinylene Carbonate) Based Solid Electrolyte with Interfacial Stability for LiCoO₂ Lithium Batteries. *Adv. Sci.* **2017**, *4*, 1600377. [[CrossRef](#)]
34. Chen, S.; Che, H.; Feng, F.; Liao, J.; Wang, H.; Yin, Y.; Ma, Z.F. Poly(vinylene carbonate)-Based Composite Polymer Electrolyte with Enhanced Interfacial Stability To Realize High-Performance Room-Temperature Solid-State Sodium Batteries. *ACS Appl. Mater. Interfaces* **2019**, *11*, 43056–43065. [[CrossRef](#)] [[PubMed](#)]
35. Zhou, M.; Liu, R.; Jia, D.; Cui, Y.; Liu, Q.; Liu, S.; Wu, D. Ultrathin Yet Robust Single Lithium-Ion Conducting Quasi-Solid-State Polymer-Brush Electrolytes Enable Ultralong-Life and Dendrite-Free Lithium-Metal Batteries. *Adv. Mater.* **2021**, *33*, e2100943. [[CrossRef](#)]
36. Zha, W.; Li, J.; Li, W.; Sun, C.; Wen, Z. Anchoring succinonitrile by solvent-Li⁺ associations for high-performance solid-state lithium battery. *Chem. Eng. J.* **2021**, *406*, 126754. [[CrossRef](#)]
37. Zha, W.; Li, W.; Ruan, Y.; Wang, J.; Wen, Z. In situ fabricated ceramic/polymer hybrid electrolyte with vertically aligned structure for solid-state lithium batteries. *Energy Storage Mater.* **2021**, *36*, 171–178. [[CrossRef](#)]
38. Yan, Y.; Ju, J.; Dong, S.; Wang, Y.; Huang, L.; Cui, L.; Jiang, F.; Wang, Q.; Zhang, Y.; Cui, G. In Situ Polymerization Permeated Three-Dimensional Li⁺-Percolated Porous Oxide Ceramic Framework Boosting All Solid-State Lithium Metal Battery. *Adv. Sci.* **2021**, *8*. [[CrossRef](#)]
39. Jiang, T.; He, P.; Wang, G.; Shen, Y.; Nan, C.W.; Fan, L.Z. Solvent-Free Synthesis of Thin, Flexible, Nonflammable Garnet-Based Composite Solid Electrolyte for All-Solid-State Lithium Batteries. *Adv. Energy Mater.* **2020**, *10*, 1903376. [[CrossRef](#)]
40. Li, Y.; Wang, Z.; Li, C.; Cao, Y.; Guo, X. Densification and ionic-conduction improvement of lithium garnet solid electrolytes by flowing oxygen sintering. *J. Power Sources* **2014**, *248*, 642–646. [[CrossRef](#)]
41. Zheng, J.; Hu, Y.Y. New Insights into the Compositional Dependence of Li-Ion Transport in Polymer-Ceramic Composite Electrolytes. *ACS Appl. Mater. Interfaces* **2018**, *10*, 4113–4120. [[CrossRef](#)] [[PubMed](#)]
42. Hu, C.; Shen, Y.; Shen, M.; Liu, X.; Chen, H.; Liu, C.; Kang, T.; Jin, F.; Li, L.; Li, J.; et al. Superionic Conductors via Bulk Interfacial Conduction. *J. Am. Chem. Soc.* **2020**, *142*, 18035–18041. [[CrossRef](#)]

43. Liu, Q.; Yang, G.; Li, X.; Zhang, S.; Chen, R.; Wang, X.; Gao, Y.; Wang, Z.; Chen, L. Polymer electrolytes based on interactions between [solvent-Li⁺] complex and solvent-modified polymer. *Energy Storage Mater.* **2022**, *51*, 443–452. [[CrossRef](#)]
44. Li, Z.; Huang, H.M.; Zhu, J.K.; Wu, J.F.; Yang, H.; Wei, L.; Guo, X. Ionic Conduction in Composite Polymer Electrolytes: Case of PEO:Ga-LLZO Composites. *ACS Appl. Mater. Interfaces* **2019**, *11*, 784–791. [[CrossRef](#)]
45. Grugeon, S.; Jankowski, P.; Cailleu, D.; Forestier, C.; Sannier, L.; Armand, M.; Johansson, P.; Laruelle, S. Towards a better understanding of vinylene carbonate derived SEI-layers by synthesis of reduction compounds. *J. Power Sources* **2019**, *427*, 77–84. [[CrossRef](#)]
46. Lim, K.; Popovic, J.; Maier, J. Ion transport and growth behavior of solid electrolyte interphases on Li and Na with liquid electrolytes based on impedance analysis. *J. Mater. Chem. A* **2023**, *11*, 5725–5733. [[CrossRef](#)]
47. Wang, Z.; Ma, J.; Cui, P.; Yao, X. High-Rate Solid Polymer Electrolyte Based Flexible All-Solid-State Lithium Metal Batteries. *ACS Appl. Mater. Interfaces* **2022**, *14*, 34649–34655. [[CrossRef](#)]
48. Barai, P.; Fuchs, T.; Trevisanello, E.; Kim, H.K.; Richter, F.H.; Janek, J.; Srinivasan, V. Reaction Current Heterogeneity at the Interface between a Lithium Electrode and Polymer/Ceramic Composite Electrolytes. *ACS Appl. Energy Mater.* **2023**, *6*, 2160–2177. [[CrossRef](#)]
49. Huo, H.; Li, X.; Chen, Y.; Liang, J.; Deng, S.; Gao, X.; Doyle-Davis, K.; Li, R.; Guo, X.; Shen, Y.; et al. Bifunctional composite separator with a solid-state-battery strategy for dendrite-free lithium metal batteries. *Energy Storage Mater.* **2020**, *29*, 361–366. [[CrossRef](#)]
50. Zhao, C.Z.; Chen, P.Y.; Zhang, R.; Chen, X.; Li, B.Q.; Zhang, X.Q.; Cheng, X.B.; Zhang, Q. An ion redistributor for dendrite-free lithium metal anodes. *Sci. Adv.* **2018**, *4*, eaat3446. [[CrossRef](#)]
51. Su, D.L.; Cui, J.; Zhai, P.B.; Guo, X.X. Mechanism Study on Garnet-type Li_{6.4}La₃Zr_{1.4}Ta_{0.6}O₁₂ Regulating the Solid Electrolyte Interphases of Si/C Anodes. *J. Inorg. Mater.* **2022**, *37*, 802–808. [[CrossRef](#)]

Disclaimer/Publisher's Note: The statements, opinions and data contained in all publications are solely those of the individual author(s) and contributor(s) and not of MDPI and/or the editor(s). MDPI and/or the editor(s) disclaim responsibility for any injury to people or property resulting from any ideas, methods, instructions or products referred to in the content.